Physics of Plasmas ARTICLE scitation.org/journal/php

Global simulation of ion temperature gradient instabilities in a field-reversed configuration

Cite as: Phys. Plasmas **26**, 042506 (2019); doi: 10.1063/1.5087079
Submitted: 27 December 2018 · Accepted: 25 March 2019 ·
Published Online: 15 April 2019

J. Bao,[1,2,3,a)] C. K. Lau,[4] Z. Lin,[1,b)] H. Y. Wang,[1,5] D. P. Fulton,[4] S. Dettrick,[4] and T. Tajima[4]

AFFILIATIONS

[1]University of California, Irvine, California 92697, USA
[2]Beijing National Laboratory for Condensed Matter Physics and CAS Key Laboratory of Soft Matter Physics, Institute of Physics, Chinese Academy of Sciences, Beijing 100190, China
[3]University of Chinese Academy of Sciences, Beijing 100049, China
[4]TAE Technologies, Inc., 19631 Pauling, Foothill Ranch, California 92610, USA
[5]Fusion Simulation Center, Peking University, Beijing 100871, China

[a)]jianbao0626@gmail.com
[b)]zhihongl@uci.edu

ABSTRACT

We investigate the global properties of drift waves in the beam driven field-reversed configuration (FRC), the C2-U device, in which the central FRC and its scrape-off layer (SOL) plasma are connected with the formation sections and divertors. The ion temperature gradient modes are globally connected and unstable across these regions, while they are linearly stable inside the FRC separatrix. The unstable global drift waves in the SOL show an axially varying structure that is less intense near the central FRC region and the mirror throat areas, while being more robust in the bad curvature formation exit areas.

I. INTRODUCTION

A field-reversed configuration (FRC) is an elongated prolate compact toroid (CT) with magnetic fields predominantly along the poloidal direction, which consists of a core with closed field lines and a scrape-off layer (SOL) with open field lines.[1] As a fusion reactor concept, FRC has many advantages: The average beta (the ratio between plasma kinetic pressure and magnetic energy density) is close to unity, which suggests a much cheaper fusion energy than the tokamak. The compact shape and simple geometry of FRC also lead to construction convenience and high magnetic efficiency. The SOL region extends to the device ends and forms natural divertors, which are far away from the core region and allow extraction of fusion energy without restriction. TAE Technologies, Inc. has launched a series of FRC experiments.[2–7] A significant energetic ion population generated from neutral beam injection (NBI) can suppress the macroinstability.[8,9] Meanwhile, the large orbit size effects of the energetic particle would not destabilize the microturbulence and the ion scale turbulent transport is suppressed.[10] These experimental efforts lead to the sustainment of beam-driven hot FRC plasmas for more than 5 ms in C-2U experiments, which is in the confinement regime limited by turbulent transport.

In FRC, the open field line SOL region is connected to the closed field line core region, and the turbulence in these two regions affects each other. In recent C2-U experiment, it is found that ion-scale turbulence fluctuation is suppressed in the core, while in the SOL, ion- and electron-scale turbulence is observed.[10] Thus, it is important to understand the transport mechanism in FRC for the improvement of plasma confinement. 1D and 2D magnetohydrodynamic (MHD) codes have been built up to model the global FRC transport, which requires turbulence simulation codes to provide the transport coefficients.[11–13] First-principles particle-in-cell simulation is a powerful tool to study the fusion plasmas combining with theory, which has successful applications in understanding the anomalous transport in tokamak plasmas.[14–24] For the particle-in-cell study of turbulence in FRC, some pioneer works[25–27] have been performed based on the state-of-the-art fusion plasma simulation code: Gyrokinetic Toroidal Code (GTC). GTC has been successfully applied to simulate microturbulence,[21,24] energetic particle transport,[28] Alfven eigenmodes,[29,30] and MHD instabilities[31,32] in toroidal plasmas. An upgrade to the FRC geometry in the Boozer coordinates of GTC has been carried out by Fulton *et al.*,[25,26] and local gyrokinetic particle simulation study by Lau

et al.[10,27] shows that the drift wave is stable in the FRC core due to the large orbit size, magnetic well geometry, and short electron transit length. Meanwhile, a new global particle-in-cell FRC code, ANC, has been developed by incorporating core and SOL regions across the separatrix. ANC simulations show that ion scale turbulence can spread from the SOL to the core.[33,34]

In order to study the turbulent transports globally up to the divertor region for FRC, a new GTC family code, gyrokinetic toroidal code-X (GTC-X), is developed in this work by refactoring the coordinate system and geometry of the original GTC code, i.e., change the Boozer coordinates to cylindrical coordinates and change the geometry from tokamak and stellarator to FRC. GTC-X enables the cross-separatrix simulation with a field aligned mesh covering the whole geometry of the FRC. Compared to the original GTC code, both the particle trajectory and the Poisson solver are newly written as well as the simulation grids in the GTC-X code. The GTC mixed-model OpenMP-MPI parallelization[35] is adopted in GTC-X. This paper mainly presents the numerical developments, code verification, and initial results of ion temperature gradient (ITG) modes in the global FRC geometry. GTC-X global simulations show that ITG is unstable in the SOL and stable in the core, which is consistent with previous local simulations and experimental observations. We find that the ITG mode grows along the field line direction in the SOL and shows an axial variation. The maximum amplitude of the ITG mode is in the formation region with bad curvature, while the mode amplitude is small in the central FRC region. The mode structure in the SOL is sensitive to the parallel domain size, which experiences a transition from even parity to odd parity when increasing the domain size.

This paper is organized as follows. In Sec. II, we introduce the global FRC geometry implementation. The gyrokinetic particle simulation model for FRC is described in Sec. III. The benchmark simulation results are shown in Sec. IV. In Sec. V, the global simulation of ITG modes is described. The conclusion is discussed in Sec. VI.

II. GLOBAL FRC GEOMETRY IMPLEMENTATION

In order to avoid the singularity of magnetic coordinates at the separatrix,[22,36] we adapt the cylindrical coordinate system for global FRC simulation with (R, ζ, Z), where the 3 independent unit vectors satisfy the right hand rule: $\hat{\boldsymbol{R}} \times \hat{\boldsymbol{\zeta}} \cdot \hat{\boldsymbol{Z}} = 1$. The poloidal magnetic flux ψ of FRC equilibrium and cylindrical coordinates used in GTC-X is shown in Fig. 1, which is calculated by an axisymmetric force balance FRC equilibrium solver: LR_eqMI code.[37] The equilibrium box size is normalized by the radial position of magnetic axis: $R = R_0 = 26.8$ cm, i.e., the distance between the magnetic axis and the cylinder axis. There are several mirror plugs in the SOL region aiming at decreasing the particle end loss, and the expanded divertors are located at the ends of open field lines, where we can apply the edge biasing via the plasma-gun electrodes to improve the confinement.[4] In this section, based on the characteristics of FRC equilibrium, we will introduce the algorithms used in GTC-X for global particle-in-cell modeling of FRC.

A. Magnetic field representation in cylindrical coordinates

The magnetic field and associated derivatives commonly appear in the particle dynamic equations for the simulation of magnetized plasmas; thus, it is important that the magnetic field satisfies $\nabla \cdot \boldsymbol{B} = 0$ numerically. The magnetic coordinates enable the free divergence representation for the magnetic field as $\mathbf{B} = \nabla\alpha \times \nabla\beta$, where α and β are coordinates which vary along the directions orthogonal to the magnetic field. However, magnetic coordinates fail to address the simulation containing different geometric topologies with a separatrix.[36] Thus, we apply the cylindrical coordinate system as the basic coordinates. In order to guarantee the free divergence property for the magnetic field in cylindrical coordinates, we use the poloidal magnetic flux ψ to calculate the magnetic field components and their derivatives and, thus, enforce the consistency between each component. In FRC, the equilibrium magnetic field $\mathbf{B}$ has no toroidal component and can be expressed as $\mathbf{B} = \nabla\psi \times \nabla\zeta = B_R\hat{\mathbf{R}} + B_Z\hat{\mathbf{Z}}$. The magnetic field strength in radial and axial directions can then be derived as

$$B_R = -\frac{1}{R}\frac{\partial\psi}{\partial Z} \tag{1}$$

and

$$B_Z = \frac{1}{R}\frac{\partial\psi}{\partial R}. \tag{2}$$

From equilibrium calculated by the LR_eqMI code, we can get the value of poloidal magnetic flux ψ over the whole FRC geometry on the equal space grids in the (R, Z) plane as shown in Fig. 1, and $LSR = 150$ and $LSZ = 401$ are the equilibrium radial and axial grid numbers, respectively. By using the value on coarse equilibrium grids, we can use the quadratic spline function to calculate ψ at the arbitrary location (R, Z) inside the equilibrium domain as

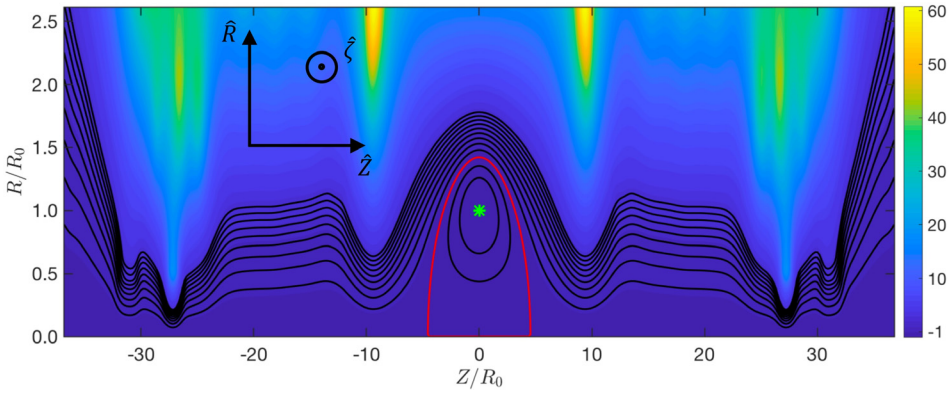

FIG. 1. Contour plot of $\psi/|\psi_O|$ for global FRC geometry, where ψ_O is the poloidal magnetic flux value at the magnetic axis as shown by the green star. The black solid lines represent the different field lines (contour line of ψ), and the red line represents the separatrix. The arrows denote the directions of cylindrical coordinates.

$$\psi(R,Z) = \psi(1,i,j) + \psi(2,i,j)\Delta R + \psi(3,i,j)\Delta R^2 + \psi(4,i,j)\Delta Z + \psi(5,i,j)\Delta R\Delta Z + \psi(6,i,j)\Delta R^2\Delta Z + \psi(7,i,j)\Delta Z^2 + \psi(8,i,j)\Delta R\Delta Z^2 + \psi(9,i,j)\Delta R^2\Delta Z^2, \quad (3)$$

where $i \in [1, LSR]$ and $j \in [1, LSZ]$ are the radial and axial indexes of equilibrium grids, and $\Delta R = R - R_i$, $\Delta Z = Z - Z_j$, $R_i \le R < R_{i+1}$ and $Z_j \le Z < Z_{j+1}$.

It is straightforward to show that $\nabla \cdot \boldsymbol{B} = 0$ is guaranteed theoretically and numerically

$$\nabla \cdot \boldsymbol{B} = \frac{1}{R}\frac{\partial}{\partial R}(RB_R) + \frac{\partial B_Z}{\partial Z} = 0. \quad (4)$$

B. Field line coordinates for the perturbed field calculation

In magnetized plasmas, the gyrocenter drift motion across the magnetic field is much slower than the parallel motion along the field line; thus, the wave pattern is always anisotropic in the parallel and perpendicular directions with $k_{||} \ll k_\perp$ ($k_{||}$ and $k_\perp$ are the parallel and perpendicular wave vectors). In order to improve the numerical efficiency and accuracy, the field aligned mesh is widely adapted for particle-in-cell simulation of magnetized plasmas, i.e., the grids are aligned along the magnetic field direction with only a small number in the parallel direction, which can dramatically suppress the high $k_{||}$ noise and save computational cost without sacrificing key physics dominated by small $k_{||}$.[23,38] In global FRC simulation, we setup a field aligned mesh in both core and scrape-off layer (SOL) regions across the separatrix in cylindrical coordinates. Due to the fact that the magnetic field is not uniform in FRC, the field aligned mesh is not regular in cylindrical coordinates. For solving perturbed fields as well as particle-grid gather-scatter operation, we create the field line coordinates for core (ψ, S_c) and SOL (ψ, S_S) regions on the poloidal plane, separately, where S_c and S_S represent the normalized field line distances along the magnetic field line direction in core and SOL regions, and the mesh is regular in the corresponding field line coordinates. Thus, in GTC-X, we use two different coordinate systems: cylindrical coordinates and field line coordinates to represent the location.

The simulation domain is different from equilibrium shown in Fig. 1. Because drift wave instabilities and associated transports are anisotropic in perpendicular and parallel directions, we choose the simulation domain based on perpendicular coordinates ψ (we do not need to consider about ζ domain because it is toroidally symmetric from $(0, 2\pi)$), i.e., the inner boundary in the core and the outer boundary in SOL are labeled by poloidal magnetic flux: ψ_0 and ψ_1. Furthermore, left and right boundaries in the SOL region are given by Z_0 and Z_1, where $Z_0 = -Z_1$ is symmetric with respect to outer midplane $Z = 0$.

First, we define S_c and S_S by tracing each field line on each ψ grid in the core and SOL regions as

$$\psi(i_c) = \psi_0 + \delta\psi_c \times (i_c - 1),$$

where $\delta\psi_c = (\psi_X - \psi_0)/(lspc - 1)$, ψ_X is the value of ψ at the separatrix, $lspc$ is the spline resolution in the core region, and $1 \le i_c \le lspc$. And

$$\psi(i_S) = \psi_X + \delta\psi_S \times (i_S - 1),$$

where $\delta\psi_S = (\psi_1 - \psi_X)/(lsps - 1)$, $lsps$ is the spline resolution in SOL region, and $1 \le i_S \le lsps$. Both S_c and S_S are normalized by the field line length at each ψ grid and range from 0 to 1. In the core region, S_c starts at the outer midplane with $Z = 0$ and increases along the clockwise direction, and grids at $S_c = 0$ and $S_c = 1$ are overlapped. In the SOL region, the parallel coordinate S_S starts on the left boundary Z_0 and ends on the right boundary Z_1.

Next, considering the properties of geometry topology of core and SOL regions in FRC, forward spline functions $S_c = S_c[\psi(R,Z), \theta(R,Z)]$ and $S_S = S_S[\psi(R,Z), Z]$ are created for the transformation from cylindrical coordinates to field line coordinates, where $\sin(\theta) = Z/\sqrt{Z^2 + (R - R_0)^2}$ is the geometric angle with respect to the magnetic axis position $(R = R_0, Z = 0)$. The uniform scale of geometric angle θ for creating spline function $S_c(\psi, \theta)$ is

$$\theta(j_c) = \delta\theta \times (j_c - 1),$$

where $\delta\theta = 2\pi/(lstc - 1)$, $lstc$ is the spline resolution in the θ direction, and $1 \le j_c \le lstc$. By tracing each field line and calculating the S_c value on the uniform scales of ψ and θ, the spline function $S_c(\psi, \theta)$ can be derived as

$$S_c(\psi,\theta) = S_c(1,i_c,j_c) + S_c(2,i_c,j_c)\Delta\psi + S_c(3,i_c,j_c)\Delta\psi^2 + S_c(4,i_c,j_c)\Delta\theta + S_c(5,i_c,j_c)\Delta\psi\Delta\theta + S_c(6,i_c,j_c)\Delta\psi^2\Delta\theta + S_c(7,i_c,j_c)\Delta\theta^2 + S_c(8,i_c,j_c)\Delta\psi\Delta\theta^2 + S_c(9,i_c,j_c)\Delta\psi^2\Delta\theta^2. \quad (5)$$

The uniform scale of Z for creating spline function $S_S(\psi, Z)$ is

$$Z(j_S) = \delta Z_S \times (j_S - 1),$$

where $\delta Z_S = (Z_1 - Z_0)/(lszs - 1)$, $lszs$ is the spline resolution in the Z direction, and $1 \le j_S \le lszs$. By tracing each field line and calculating the S_S value on the uniform scales of ψ and Z, $S_S(\psi, Z)$ is given as

$$S_S(\psi,Z) = S_S(1,i_S,j_S) + S_S(2,i_S,j_S)\Delta\psi + S_S(3,i_S,j_S)\Delta\psi^2 + S_S(4,i_S,j_S)\Delta Z + S_S(5,i_S,j_S)\Delta\psi\Delta Z + S_S(6,i_S,j_S)\Delta\psi^2\Delta Z + S_S(7,i_S,j_S)\Delta Z^2 + S_S(8,i_S,j_S)\Delta\psi\Delta Z^2 + S_S(9,i_S,j_S)\Delta\psi^2\Delta Z^2. \quad (6)$$

Then, we create the inverse spline functions $R_c(\psi, S_c)$ and $Z_c(\psi, S_c)$ for the core region, and $R_S(\psi, S_S)$ and $Z_S(\psi, S_S)$ for the SOL region. The uniform scales of S_c and S_S for the spline function are

$$S_c(j_c) = \delta S_c \times (j_c - 1),$$

where $\delta S_c = 1/(lssc - 1)$, $lssc$ is the spline resolution in the parallel direction in the core region, and $1 \le j_c \le lssc$

$$S_S(j_S) = \delta S_S \times (j_S - 1),$$

where $\delta S_S = 1/(lsss - 1)$, $lsss$ is the spline resolution in the parallel direction in the SOL region, and $1 \le j_S \le lsss$. It is straightforward to get the values $R_c[\psi(i_c), S_c(j_c)]$, $Z_c[\psi(i_c), S_c(j_c)]$, $R_S[\psi(i_S), S_S(j_S)]$, and $Z_S[\psi(i_S), S_S(j_S)]$ on the uniform scales of (ψ, S_c) and (ψ, S_S), and the quadratic spline functions $R_c(\psi, S_c)$, $Z_c(\psi, S_c)$, $R_S(\psi, S_S)$, and $Z_S(\psi, S_S)$ can then be created as

$$R_c(\psi,S_c) = R_c(1,i_c,j_c) + R_c(2,i_c,j_c)\Delta\psi + R_c(3,i_c,j_c)\Delta\psi^2 + R_c(4,i_c,j_c)\Delta S + R_c(5,i_c,j_c)\Delta\psi\Delta S + R_c(6,i_c,j_c)\Delta\psi^2\Delta S + R_c(7,i_c,j_c)\Delta S^2 + R_c(8,i_c,j_c)\Delta\psi\Delta S^2 + R_c(9,i_c,j_c)\Delta\psi^2\Delta S^2, \quad (7)$$

and

$$Z_c(\psi,S_c)=Z_c(1,i_c,j_c)+Z_c(2,i_c,j_c)\Delta\psi+Z_c(3,i_c,j_c)\Delta\psi^2 +Z_c(4,i_c,j_c)\Delta S+Z_c(5,i_c,j_c)\Delta\psi\Delta S+Z_c(6,i_c,j_c)\Delta\psi^2\Delta S +Z_c(7,i_c,j_c)\Delta S^2+Z_c(8,i_c,j_c)\Delta\psi\Delta S^2+Z_c(9,i_c,j_c)\Delta\psi^2\Delta S^2, \tag{8}$$

where $\Delta\psi=\psi-\psi(i_c)$ and $\Delta S=S_c-S(j_c)$. $\psi(i_c)\le\psi<\psi(i_c+1)$, and $S(j_c)\le S_c<S(j_c+1)$.

$$R_S(\psi,S_S)=R_S(1,i_S,j_S)+R_S(2,i_S,j_S)\Delta\psi+R_S(3,i_S,j_S)\Delta\psi^2 +R_S(4,i_S,j_S)\Delta S+R_S(5,i_S,j_S)\Delta\psi\Delta S+R_S(6,i_S,j_S)\Delta\psi^2\Delta S +R_S(7,i_S,j_S)\Delta S^2+R_S(8,i_S,j_S)\Delta\psi\Delta S^2+R_S(9,i_S,j_S)\Delta\psi^2\Delta S^2, \tag{9}$$

and

$$Z_S(\psi,S_S)=Z_S(1,i_S,j_S)+Z_S(2,i_S,j_S)\Delta\psi+Z_S(3,i_S,j_S)\Delta\psi^2 +Z_S(4,i_S,j_S)\Delta S+Z_S(5,i_S,j_S)\Delta\psi\Delta S+Z_S(6,i_S,j_S)\Delta\psi^2\Delta S +Z_S(7,i_S,j_S)\Delta S^2+Z_S(8,i_S,j_S)\Delta\psi\Delta S^2+Z_S(9,i_S,j_S)\Delta\psi^2\Delta S^2, \tag{10}$$

where $\Delta\psi=\psi-\psi(i_S)$ and $\Delta S=S_S-S(j_S)$. $\psi(i_S)\le\psi<\psi(i_S+1)$ and $S(j_S)\le S_S<S(j_S+1)$.

By using Eqs. (7)–(10), we could compute the field aligned mesh in cylindrical coordinates with a given regular mesh in the core region (ψ,S_c) and in the SOL region (ψ,S_S), respectively. An example of global field aligned mesh is given in Fig. 2(a). The field aligned grids are irregular in cylindrical coordinates. For the overlap part of core and SOL regions at the separatrix ($R>0$), the grid positions are determined by using $R_c(\psi,S_c)$ and $Z_c(\psi,S_c)$, which are shared by both core and SOL regions with the scopes of two coordinates: (ψ,S_c) and (ψ,S_S) as shown by the black stars. In magnetic coordinates, the grids in SOL and core regions are regular inside each domain, respectively. The shared grids at the separatrix are designed regularly with the interior grids in the core region (keep the same parallel coordinate S_c value), which are shown in Figs. 2(b) and 2(c).

In GTC-X, particle dynamic equations are evolved in cylindrical coordinates (R,ζ,Z) to avoid the singularity at the separatrix. However, the field aligned mesh is irregular in (R, Z) space, which is difficult to carry out particle-grid gather-scatter operation for PIC simulation. It is noted that the field aligned grids are labeled by both cylindrical and magnetic coordinates: (R, Z) and (ψ,S_c) in the core region and (R, Z) and (ψ,S_S) in the SOL region. The mesh is regular in magnetic coordinates in the core and SOL regions, respectively, as shown in Fig. 2. Thus, we can transform the particle coordinate from (R, Z) to (ψ,S_c) and (ψ,S_S) by using Eqs. (3), (5), and (6), and then a simple linear interpolation between the particle location and the regular rectangular mesh can be used for particle-grid gather-scatter operation,

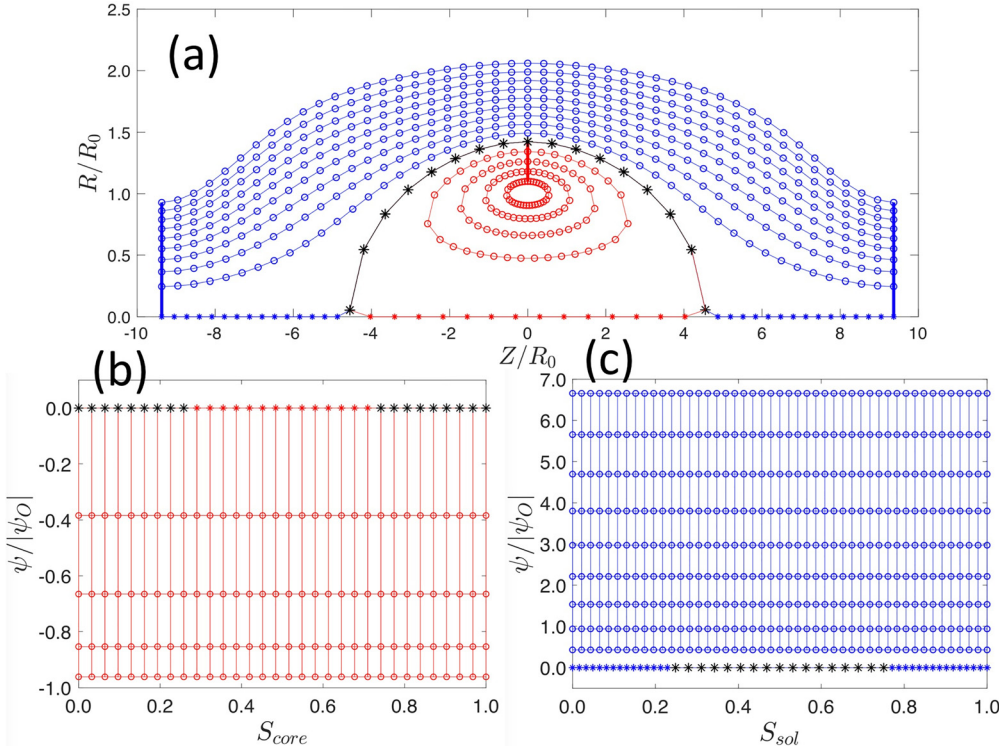

FIG. 2. (a) Global field aligned mesh in cylindrical coordinates. Field aligned mesh mapping from cylindrical coordinates to magnetic coordinates: (b) core region grids in (ψ,S_c) coordinates and (c) SOL region grids in (ψ,S_S) coordinates. The black stars represent the shared grids at the separatrix. The grids shown here are only for illustrating the algorithm, which are much sparser than the ones used in realistic simulation.

where we implement 3 1D linear interpolations along ψ, ζ, and S_c/S_S for the simulations in 3 dimensional $(\psi, \zeta, S_c/S_S)$ space.

C. Laplacian operator

In the global simulation of FRC geometry with the field aligned mesh, the perpendicular Laplacian operator is discretized in (ψ, ζ, S_c) space for the core region and in (ψ, ζ, S_S) space for the SOL region, respectively, since the irregular mesh in cylindrical coordinates becomes regular in magnetic coordinates.

The Laplacian operator can be expanded in a generalized coordinates

$$\nabla^2 f = \frac{1}{J}\frac{\partial}{\partial \xi^\alpha}\left(J\nabla\xi^\alpha \cdot \nabla\xi^\beta \frac{\partial f}{\partial \xi^\beta}\right), \tag{11}$$

where f represents an arbitrary scalar field, ξ^α, ξ^β refer to the three dimensional coordinates, and J is Jacobian and defined as $J^{-1}\epsilon^{\alpha\beta\gamma} = \nabla\xi^\alpha \times \nabla\xi^\beta \cdot \nabla\xi^\gamma$, $\nabla\xi^\alpha = \frac{\partial \xi^\alpha}{\partial R}\hat{R} + \frac{\partial \xi^\alpha}{\partial \zeta}\frac{1}{R}\hat{\zeta} + \frac{\partial \xi^\alpha}{\partial Z}\hat{Z}$, and $\epsilon^{\alpha\beta\gamma} = 1$, and it becomes antisymmetric when the indices change.[39]

In the core region with (ψ, ζ, S_c), considering $S_c = S_c[\psi(R,Z), \theta(R,Z)]$, the Laplacian is written as

$$\begin{aligned}\nabla_c^2 f = {} & g^{\psi\psi}\frac{\partial^2 f}{\partial \psi^2} + 2g_c^{\psi S}\frac{\partial^2 f}{\partial \psi \partial S_c} + g_c^{SS}\frac{\partial^2 f}{\partial S_c^2} + g^{\zeta\zeta}\frac{\partial^2 f}{\partial \zeta^2} \\ & + \frac{1}{J_c}\left[\frac{\partial\left(J_c g^{\psi\psi}\right)}{\partial \psi} + \frac{\partial\left(J_c g_c^{\psi S}\right)}{\partial S_c}\right]\frac{\partial f}{\partial \psi} \\ & + \frac{1}{J_c}\left[\frac{\partial\left(J_c g_c^{\psi S}\right)}{\partial \psi} + \frac{\partial\left(J_c g_c^{SS}\right)}{\partial S_c}\right]\frac{\partial f}{\partial S_c},\end{aligned} \tag{12}$$

where

$$\begin{aligned} J_c^{-1} &= \nabla\psi \times \nabla\zeta \cdot \nabla S_c \\ &= \left(\frac{\partial\psi}{\partial R}\hat{R} + \frac{\partial\psi}{\partial Z}\hat{Z}\right) \times \frac{1}{R}\hat{\zeta} \cdot \left[\frac{\partial S_c}{\partial \psi}\left(\frac{\partial\psi}{\partial R}\hat{R} + \frac{\partial\psi}{\partial Z}\hat{Z}\right)\right. \\ &\quad \left. + \frac{\partial S_c}{\partial \theta}\left(\frac{\partial\theta}{\partial R}\hat{R} + \frac{\partial\theta}{\partial Z}\hat{Z}\right)\right] \\ &= \frac{1}{R}\frac{\partial\psi}{\partial R}\frac{\partial S_c}{\partial\theta}\frac{\partial\theta}{\partial Z} - \frac{1}{R}\frac{\partial\psi}{\partial Z}\frac{\partial S_c}{\partial\theta}\frac{\partial\theta}{\partial R}, \end{aligned}$$

$$g^{\psi\psi} = \nabla\psi \cdot \nabla\psi = \left(\frac{\partial\psi}{\partial R}\right)^2 + \left(\frac{\partial\psi}{\partial Z}\right)^2,$$

$$g_c^{SS} = \nabla S_c \cdot \nabla S_c = \left(\frac{\partial S_c}{\partial\psi}\frac{\partial\psi}{\partial R} + \frac{\partial S_c}{\partial\theta}\frac{\partial\theta}{\partial R}\right)^2 + \left(\frac{\partial S_c}{\partial\psi}\frac{\partial\psi}{\partial Z} + \frac{\partial S_c}{\partial\theta}\frac{\partial\theta}{\partial Z}\right)^2,$$

$$\begin{aligned} g_c^{\psi S} &= \nabla\psi \cdot \nabla S_c \\ &= \frac{\partial S_c}{\partial\psi}\left[\left(\frac{\partial\psi}{\partial R}\right)^2 + \left(\frac{\partial\psi}{\partial Z}\right)^2\right] + \frac{\partial S_c}{\partial\theta}\left[\frac{\partial\psi}{\partial R}\frac{\partial\theta}{\partial R} + \frac{\partial\psi}{\partial Z}\frac{\partial\theta}{\partial Z}\right], \end{aligned}$$

$$g^{\zeta\zeta} = \nabla\zeta \cdot \nabla\zeta = \frac{1}{R^2}.$$

In the SOL region with (ψ, ζ, S_S), considering $S_S = S_S[\psi(R,Z), Z]$, the Laplacian is written as

$$\begin{aligned}\nabla_S^2 f = {} & g^{\psi\psi}\frac{\partial^2 f}{\partial \psi^2} + 2g_S^{\psi S}\frac{\partial^2 f}{\partial \psi \partial S_S} + g_S^{SS}\frac{\partial^2 f}{\partial S_S^2} + g^{\zeta\zeta}\frac{\partial^2 f}{\partial \zeta^2} \\ & + \frac{1}{J_S}\left[\frac{\partial\left(J_S g^{\psi\psi}\right)}{\partial \psi} + \frac{\partial\left(J_S g_S^{\psi S}\right)}{\partial S_S}\right]\frac{\partial f}{\partial \psi} \\ & + \frac{1}{J_S}\left[\frac{\partial\left(J_S g_S^{\psi S}\right)}{\partial \psi} + \frac{\partial\left(J_S g_S^{SS}\right)}{\partial S_S}\right]\frac{\partial f}{\partial S_S},\end{aligned} \tag{13}$$

where

$$\begin{aligned} J_S^{-1} &= \nabla\psi \times \nabla\zeta \cdot \nabla S_S \\ &= \left(\frac{\partial\psi}{\partial R}\hat{R} + \frac{\partial\psi}{\partial Z}\hat{Z}\right) \times \frac{1}{R}\hat{\zeta} \cdot \left[\frac{\partial S_S}{\partial\psi}\left(\frac{\partial\psi}{\partial R}\hat{R} + \frac{\partial\psi}{\partial Z}\hat{Z}\right) + \frac{\partial S_S}{\partial Z}\hat{Z}\right] \\ &= \frac{1}{R}\frac{\partial\psi}{\partial R}\frac{\partial S_S}{\partial Z}, \end{aligned}$$

$$g_S^{SS} = \nabla S_S \cdot \nabla S_S = \left(\frac{\partial S_S}{\partial\psi}\frac{\partial\psi}{\partial R}\right)^2 + \left(\frac{\partial S_S}{\partial\psi}\frac{\partial\psi}{\partial Z} + \frac{\partial S_S}{\partial Z}\right)^2,$$

$$g_S^{\psi S} = \nabla\psi \cdot \nabla S_S = \frac{\partial S_S}{\partial\psi}\left[\left(\frac{\partial\psi}{\partial R}\right)^2 + \left(\frac{\partial\psi}{\partial Z}\right)^2\right] + \frac{\partial\psi}{\partial Z}\frac{\partial S_S}{\partial Z}.$$

For the shared grids between core and SOL regions at the separatrix, the perpendicular Laplacian operator is expanded as

$$\nabla_{\perp,X}^2 f = g^{\psi\psi}\frac{\partial^2 f}{\partial\psi^2}\Big|_{b_0\times\zeta} + \frac{1}{J_X}\frac{\partial J_X g^{\psi\psi}}{\partial\psi}\frac{\partial f}{\partial\psi}\Big|_{b_0\times\zeta} + g^{\zeta\zeta}\frac{\partial^2 f}{\partial\zeta^2}, \tag{14}$$

where $|_{b_0\times\zeta}$ represents the partial derivative with respect to ψ among the orthogonal grids along the $\boldsymbol{b}_0 \times \zeta$ direction, and

$$\begin{aligned} J_X^{-1} &= \nabla\psi \times \nabla\zeta \cdot \nabla S_X \\ &= \left(\frac{\partial\psi}{\partial R}\hat{R} + \frac{\partial\psi}{\partial Z}\hat{Z}\right) \times \frac{1}{R}\hat{\zeta} \cdot \left[\frac{\partial S_X}{\partial R}\hat{R} + \frac{\partial S_X}{\partial Z}\hat{Z}\right] \\ &= \frac{1}{R}\frac{\partial\psi}{\partial R}\frac{\partial S_X}{\partial Z} - \frac{1}{R}\frac{\partial\psi}{\partial Z}\frac{\partial S_X}{\partial R}. \end{aligned}$$

Taking advantage of the toroidal symmetry of FRC, we could transform the Laplacian operator into Fourier space with respect to the toroidal angle ζ, which can avoid solving the 3 dimensional matrix. In this paper, we can also simplify Eqs. (12)–(14) assuming $k_\perp \gg \kappa$ and $k_{||} \ll k_\perp$, where $\kappa = \nabla B_0/B_0$. Thus, for each toroidal mode n $(\partial/\partial\zeta = in\zeta)$, the Laplacian operators in the core region, SOL region, and at the separatrix can be written as

$$\nabla_{\perp c}^2 f_n \approx g^{\psi\psi}\frac{\partial^2 f_n}{\partial\psi^2} + 2g_c^{\psi S}\frac{\partial^2 f_n}{\partial\psi\partial S_c} + g_c^{SS}\frac{\partial^2 f_n}{\partial S_c^2} - n^2 g^{\zeta\zeta} f_n, \tag{15}$$

$$\nabla_{\perp S}^2 f_n \approx g^{\psi\psi}\frac{\partial^2 f_n}{\partial\psi^2} + 2g_S^{\psi S}\frac{\partial^2 f_n}{\partial\psi\partial S_S} + g_S^{SS}\frac{\partial^2 f_n}{\partial S_S^2} - n^2 g^{\zeta\zeta} f_n, \tag{16}$$

$$\nabla_{\perp X}^2 f_n \approx g^{\psi\psi}\frac{\partial^2 f_n}{\partial\psi^2}\Big|_{b_0\times\zeta} - n^2 g^{\zeta\zeta} f_n, \tag{17}$$

where f_n is the n toroidal mode component of f.

The grids shown in Figs. 2 and 3 are only for illustrating the field aligned grid algorithm in cylindrical coordinates clearly, which are much sparser than the realistic simulation.

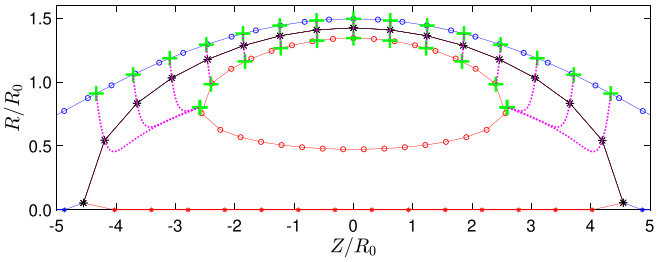

FIG. 3. The green + symbols denote the orthogonal grids in the SOL and core regions with respect to the shared grids at the separatrix, and the dotted line in magenta is along the perpendicular direction $\mathbf{b}_0 \times \hat{\zeta}$ from the shared grids as shown by the black stars. The grids shown here are only for illustrating the algorithm, which are much sparser than the ones used in realistic simulation.

III. PHYSICS MODEL

A. Formulation

We use the electrostatic Vlasov-Poisson system for physics simulation in this paper. Particle dynamics is described by the gyrokinetic equation using gyrocenter position $\boldsymbol{R}$, magnetic moment μ, and parallel velocity $v_{||}$ as independent variables in five dimensional phase space

$$\left(\frac{\partial}{\partial t} + \dot{\boldsymbol{R}} \cdot \nabla + \dot{v}_{||} \frac{\partial}{\partial v_{||}}\right) f_\alpha(\boldsymbol{R}, v_{||}, \mu, t) = 0, \tag{18}$$

$$\dot{\boldsymbol{R}} = v_{||}\boldsymbol{b} + \boldsymbol{v}_{\boldsymbol{E}} + \boldsymbol{v}_{\boldsymbol{d}}, \tag{19}$$

$$\dot{v}_{||} = -\frac{1}{m_\alpha}\frac{\boldsymbol{B}^*}{B^*_{||}} \cdot (Z_\alpha \nabla\langle\delta\phi\rangle + \mu\nabla B), \tag{20}$$

where Z_α, m_α, and f_α are the charge, mass, and distribution function of α species. $\boldsymbol{B}$ is the equilibrium magnetic field, $\boldsymbol{b} = \boldsymbol{B}/B$, $\boldsymbol{B}^* = \boldsymbol{B} + (Bv_{||}/\Omega_{c\alpha})\nabla \times \boldsymbol{b}$, and $B^*_{||} = \boldsymbol{b} \cdot \boldsymbol{B}^*$. $\delta\phi$ is the electrostatic potential. $\langle\cdots\rangle = (1/2\pi)\int \boldsymbol{dx}d\xi(\cdots)\delta(\boldsymbol{R} + \boldsymbol{\rho_\alpha} - \boldsymbol{x})$ represents the gyrophase average, ξ is the gyrophase angle, $\boldsymbol{x}$ represents the particle position, $\boldsymbol{\rho_\alpha} = \boldsymbol{b} \times \boldsymbol{v}_\perp/\Omega_{c\alpha}$ is the particle gyroradius, and $\Omega_{c\alpha}$ is the particle cyclotron frequency. $\boldsymbol{v}_{\boldsymbol{E}}$ is the $\boldsymbol{E} \times \boldsymbol{B}$ velocity, and $\boldsymbol{v}_{\boldsymbol{d}}$ is the magnetic drift velocity, which are given as

$$\boldsymbol{v}_{\boldsymbol{E}} = \frac{c\boldsymbol{b} \times \nabla\langle\delta\phi\rangle}{B^*_{||}},$$

$$\boldsymbol{v}_{\boldsymbol{d}} = \frac{cm_\alpha v^2_{||}}{Z_\alpha B^*_{||}}\boldsymbol{b} \times (\boldsymbol{b} \cdot \nabla\boldsymbol{b}) + \frac{c\mu}{Z_\alpha B^*_{||}}\boldsymbol{b} \times \nabla B.$$

In order to minimize the particle noise, the perturbative δf simulation method[16,17] is applied. The particle distribution is decomposed into equilibrium and perturbed parts as $f_\alpha = f_{\alpha 0}(\boldsymbol{R}, \mu, v_{||}) + \delta f_\alpha(\boldsymbol{R}, \mu, v_{||}, t)$, and the equilibrium $f_{\alpha 0}$ satisfies the following equation:

$$L_0 f_{\alpha 0} = 0, \tag{21}$$

where $L_0 = \partial/\partial t + (v_{||}\boldsymbol{b} + \boldsymbol{v}_{\boldsymbol{d}}) \cdot \nabla - (\mu/m_\alpha)\boldsymbol{B}^* \cdot \nabla B/B^*_{||}(\partial/\partial v_{||})$. Because $\boldsymbol{v}_{\boldsymbol{d}}$ is only in the $\hat{\zeta}$ direction, the particle drift orbit width is zero in FRC geometry, then $f_{\alpha 0} = n_{\alpha 0}(\frac{m_\alpha}{2\pi T_{\alpha 0}})^{1.5}\exp[-\frac{m_\alpha v^2_{||} + 2\mu B}{2T_{\alpha 0}}]$ is the exact solution of Eq. (21), and $n_{\alpha 0}(\psi)$ and $T_{\alpha 0}(\psi)$ are the 1D function of magnetic flux surface. Subtracting Eq. (18) by Eq. (21), we have the equation for perturbed distribution δf_α

$$L\delta f_\alpha = -\delta L f_{\alpha 0}, \tag{22}$$

where $\delta L = \boldsymbol{v}_{\boldsymbol{E}} \cdot \nabla - (Z_\alpha/m_\alpha/B^*_{||})\boldsymbol{B}^* \cdot \nabla\langle\delta\phi\rangle(\partial/\partial v_{||})$ and $L = L_0 + \delta L$. Defining particle weight as $w_\alpha = \delta f_\alpha/f_\alpha$, we can derive the weight equation from Eq. (22) as

$$\frac{dw_\alpha}{dt} = (1 - w_\alpha)\left[-\boldsymbol{v}_{\boldsymbol{E}} \cdot \frac{\nabla f_{\alpha 0}}{f_{\alpha 0}}\bigg|_{v_\perp} - \frac{Z_\alpha v_{||}\boldsymbol{b} \cdot \nabla\langle\delta\phi\rangle}{T_{\alpha 0}} - \frac{Z_\alpha}{T_{\alpha 0}}\left(\frac{\mu\boldsymbol{b} \times \nabla B_0}{m_\alpha\Omega_{c\alpha}} + \frac{v^2_{||}}{\Omega_{c\alpha}}\boldsymbol{b} \times (\boldsymbol{b} \cdot \nabla\boldsymbol{b})\right) \cdot \nabla\langle\delta\phi\rangle\right], \tag{23}$$

where we have used the chain rule $\nabla f_{\alpha 0}|_{v_\perp} = \nabla f_{\alpha 0}|_\mu + (\mu f_{\alpha 0}\nabla B/T_{\alpha 0})$ in the derivation of Eq. (23) from Eq. (22).

The gyrokinetic Vlasov equation is used for ion species, and its perturbed density is

$$\langle\delta n_i(\boldsymbol{x}, t)\rangle = \int \delta f_i(\boldsymbol{R}, \mu, v_{||}, t)\boldsymbol{dv}\boldsymbol{dR}d\xi\delta(\boldsymbol{R} + \boldsymbol{\rho_i} - \boldsymbol{x})/(2\pi). \tag{24}$$

Electron dynamics is assumed as adiabatic for simplicity, and the electron perturbed density is

$$\delta n_e(\boldsymbol{x}, t) = \frac{e\delta\phi}{T_{e0}}n_{e0}. \tag{25}$$

The gyrokinetic Poisson's equation is[14]

$$\frac{Z_i^2 n_{i0}}{T_{i0}}\left(\delta\phi - \widetilde{\delta\phi}\right) = Z_i\langle\delta n_i\rangle - e\delta n_e, \tag{26}$$

where n_{i0} and T_{i0} are the equilibrium ion density and temperature. $\widetilde{\delta\phi}$ is the double gyrophase average of electrostatic potential for ion species, which is given as

$$\widetilde{\delta\phi}(\boldsymbol{x}, t) = \frac{1}{n_{i0}}\int f_{i0}(\boldsymbol{R}, \mu, v_{||})\langle\delta\phi\rangle\boldsymbol{dv}\boldsymbol{dR}d\xi\delta(\boldsymbol{R} + \boldsymbol{\rho_i} - \boldsymbol{x})/(2\pi), \tag{27}$$

where $\int \boldsymbol{dv} = \frac{2\pi B}{m_i}\int dv_{||}d\mu$.

B. Implementation of dynamic equations in cylindrical coordinates

The gyrocenter equation of motion is

$$\dot{\mathbf{R}} = \underbrace{v_{||}\mathbf{b}}_{\{parallel\ motion\}} \underbrace{+\frac{v^2_{||}}{\Omega_{c\alpha}}\nabla \times \mathbf{b}}_{\{curvature\ drift\}} + \underbrace{\frac{\mu\mathbf{b} \times \nabla B}{m_\alpha\Omega_{c\alpha}}}_{\{grad-B\ drift\}} + \underbrace{\frac{c\mathbf{b} \times \nabla\langle\delta\phi\rangle}{B}}_{\{E\times B\ drift\}}, \tag{28}$$

with

$$\underbrace{v_{||}\mathbf{b}}_{\{parallel\ motion\}} = v_{||}(b_R\hat{\mathbf{R}} + b_Z\hat{\mathbf{Z}}),$$

$$\underbrace{\frac{v^2_{||}}{\Omega_{c\alpha}}\nabla \times \mathbf{b}}_{\{curvature\ drift\}} = \left[\frac{1}{m_\alpha\Omega_{c\alpha}}\frac{m_\alpha v^2_{||}}{B}\left(b_Z\frac{\partial B}{\partial R} - b_R\frac{\partial B}{\partial Z}\right) + \frac{v^2_{||}}{\Omega_{c\alpha}B}\left(\frac{\partial B_R}{\partial Z} - \frac{\partial B_Z}{\partial R}\right)\right]\hat{\boldsymbol{\zeta}},$$

$$\underbrace{\frac{\mu\mathbf{b}\times\nabla B}{m_\alpha\Omega_{c\alpha}}}_{\{grad-B\,drift\}}=\frac{\mu}{m_\alpha\Omega_{c\alpha}}\left(b_Z\frac{\partial B}{\partial R}-b_R\frac{\partial B}{\partial Z}\right)\hat{\boldsymbol{\zeta}},$$

$$\underbrace{\frac{c\mathbf{b}\times\nabla\langle\delta\phi\rangle}{B}}_{E\times B\,drift}=\frac{c}{B}\left[-\frac{1}{R}b_Z\frac{\partial\langle\delta\phi\rangle}{\partial\zeta}\hat{\mathbf{R}}+\left(b_Z\frac{\partial\langle\delta\phi\rangle}{\partial R}-b_R\frac{\partial\langle\delta\phi\rangle}{\partial Z}\right)\hat{\boldsymbol{\zeta}}+\frac{1}{R}b_R\frac{\partial\langle\delta\phi\rangle}{\partial\zeta}\hat{\mathbf{Z}}\right],$$

and

$$\begin{aligned}\dot{v}_{||}&=-\frac{1}{m_\alpha}\frac{1}{B}\left(\mathbf{B}+\frac{Bv_{||}}{\Omega_{c\alpha}}\nabla\times\mathbf{b}\right)\cdot(Z_\alpha\nabla\langle\delta\phi\rangle+\mu\nabla B)\\&=\underbrace{-\frac{1}{m_\alpha}\mathbf{b}\cdot(Z_\alpha\nabla\langle\delta\phi\rangle+\mu\nabla B)}_{\{I\}}\underbrace{-\frac{1}{m_\alpha}\frac{v_{||}}{\Omega_{c\alpha}}\nabla\times\mathbf{b}\cdot(Z_\alpha\nabla\langle\delta\phi\rangle+\mu\nabla B)}_{\{II\}}\\&=\underbrace{-\frac{Z_\alpha}{m_\alpha}\frac{\partial\langle\delta\phi\rangle}{\partial S}-\frac{\mu}{m_\alpha}\left(b_R\frac{\partial B}{\partial R}+b_Z\frac{\partial B}{\partial Z}\right)}_{\{I\}}\\&\quad\underbrace{-\frac{Z_\alpha}{m_\alpha}\frac{v_{||}}{\Omega_{c\alpha}}\frac{1}{R}\frac{\partial\langle\delta\phi\rangle}{\partial\zeta}\left[\left(b_Z\frac{\partial B}{\partial R}-b_R\frac{\partial B}{\partial Z}\right)+\left(\frac{\partial B_R}{\partial Z}-\frac{\partial B_Z}{\partial R}\right)\right]}_{\{II\}}.\end{aligned}\tag{29}$$

The weight equation is

$$\frac{dw_i}{dt}=(1-w_i)\left(\underbrace{-\boldsymbol{v}_{\boldsymbol{E}}\cdot\frac{\nabla f_{i0}}{f_{i0}}\bigg|_{v_\perp}}_{wdrive}+\underbrace{\frac{Z_i}{T_{i0}}v_{||}E_{||}}_{wpara}+\underbrace{\frac{Z_i}{T_{i0}}\boldsymbol{v}_{\boldsymbol{d}}\cdot\boldsymbol{E}_\perp}_{wdrift}\right),\tag{30}$$

where

$$\begin{aligned}\underbrace{-\boldsymbol{v}_{\boldsymbol{E}}\cdot\frac{\nabla f_{i0}}{f_{i0}}\bigg|_{v_\perp}}_{wdrive}&=\frac{c}{B_0}b_Z\frac{1}{R}\frac{\partial\langle\delta\phi\rangle}{\partial\zeta}\left[\frac{1}{n_{i0}}\frac{\partial n_{i0}}{\partial R}+\left(\frac{\epsilon}{T_{i0}}-1.5\right)\frac{1}{T_{i0}}\frac{\partial T_{i0}}{\partial R}\right]\\&\quad-\frac{c}{B_0}b_R\frac{1}{R}\frac{\partial\langle\delta\phi\rangle}{\partial\zeta}\left[\frac{1}{n_{i0}}\frac{\partial n_{i0}}{\partial Z}+\left(\frac{\epsilon}{T_{i0}}-1.5\right)\frac{1}{T_{i0}}\frac{\partial T_{i0}}{\partial Z}\right],\end{aligned}$$

with $\epsilon=0.5m_iv_{||}^2+\mu B$,

$$\underbrace{\frac{Z_i}{T_{i0}}v_{||}E_{||}}_{wpara}=-\frac{Z_i}{T_{i0}}v_{||}\boldsymbol{b}\cdot\nabla\langle\delta\phi\rangle=-\frac{Z_iv_{||}}{T_{i0}}\frac{\partial\langle\delta\phi\rangle}{\partial S},$$

with $S=S_c\times L$ or $S=S_S\times L$, and L is the field line length, and

$$\begin{aligned}\underbrace{\frac{Z_i}{T_{i0}}\boldsymbol{v}_{\boldsymbol{d}}\cdot\boldsymbol{E}_\perp}_{wdrift}&=-\frac{Z_i}{T_{i0}}\left(\frac{\mu\boldsymbol{b}\times\nabla B}{m_i\Omega_{ci}}+\frac{v_{||}^2}{\Omega_{c\alpha}}\nabla\times\mathbf{b}\right)\cdot\nabla\langle\delta\phi\rangle\\&=-\frac{Z_i}{T_{i0}}\frac{1}{R}\frac{1}{B}\frac{\partial\langle\delta\phi\rangle}{\partial\zeta}\left[\frac{c}{Z_i}\left(\mu+\frac{m_iv_{||}^2}{B}\right)\left(b_Z\frac{\partial B}{\partial R}-b_R\frac{\partial B}{\partial Z}\right)+\frac{v_{||}^2}{\Omega_{ci}}\left(\frac{\partial B_R}{\partial Z}-\frac{\partial B_Z}{\partial R}\right)\right].\end{aligned}$$

In GTC-X, the gyro-average is performed analytically by multiplying the fields with Bessel function as $\langle\delta\phi\rangle=\delta\phi J_0(k_\zeta\rho_i)$ and $\langle\delta n_i\rangle=\delta n_i\ J_0(k_\zeta\rho_i)$, where $\rho_i=v_{th,i}/\Omega_{ci}$ is the ion gyroradius, $v_{th,i}=\sqrt{T_i/m_i}$, $\Omega_{ci}=Z_iB/cm_i$, $k_\zeta=n/R$ is the toroidal wave vector, n is the toroidal mode number, and R is the radial position, which is only valid for single toroidal mode simulation. The radial component of perpendicular wave vector k_r is not considered for the gyro-average in the current implementation for simplicity. In the future work, a more realistic gyro-average using the 4 point average method[21] will be implemented in GTC-X for multiple mode simulation, which is used in another FRC drift wave code ANC.

The comparisons between gyrocenter and fully kinetic particle trajectories with different particle energies and locations are shown in Fig. 4. Both gyrocenter and fully kinetic particle pitch angles at the outer midplane are $\tan\theta=v_{||}/v_\perp=1$, which are trapped between two mirror throats. It is seen that gyrokinetic description is suitable for SOL region simulation with low temperature and high magnetic field, and its fidelity decreases with increasing the particle energy and moving toward the core region. Recently, a theoretical work has illustrated that the fidelity of the gyrokinetic equation is well achieved in the non-uniform magnetic field with $\epsilon=\rho/L<1$,[40] where ρ is the gyroradius and L is the magnetic field gradient scale length. With regard to FRC geometry, the gyrokinetic description of thermal ion can capture the gyro-orbit but not betatron and figure-8 orbit.[41] However, a strong finite Larmor radius effect stabilizes the drift wave instability near or inside the core region, which has been observed in experiment[10] and by previous local simulations.[25–27] Thus, in this paper, we focus on gyrokinetic simulation of ITG instability in FRC as the first step to demonstrate the code capability for GTC-X as well as reveal the global nature of ITG instability in the SOL region.

C. Poisson solver

Poisson's equation is solved in a semispectral form. Applying Padé approximation, $\widetilde{\delta\phi}\approx\frac{1}{1+k_\perp^2\rho_i^2}\delta\phi$, Eq. (26) can be written as

$$\begin{aligned}&\frac{e^2n_{i0}}{T_{e0}}\left[-\frac{Z_i^2}{e^2}\rho_s^2\left(1+\frac{e^2}{Z_i^2}\frac{n_{e0}}{n_{i0}}\frac{T_i}{T_e}\right)\nabla_\perp^2+\frac{n_{e0}}{n_{i0}}\right]\delta\psi\\&\quad=Z_i\delta n_i\frac{1}{1+\dfrac{e^2}{Z_i^2}\dfrac{n_{e0}}{n_{i0}}\dfrac{T_{i0}}{T_{e0}}},\end{aligned}\tag{31}$$

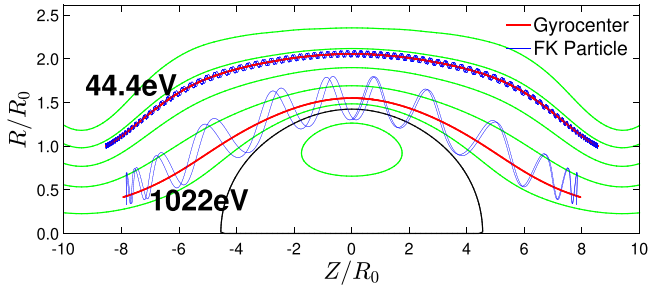

FIG. 4. Comparison of the trajectory between the fully kinetic particle and the gyrocenter for 44.4 eV and 1022 eV deuterium cases. The black solid line represents the separatrix, and green solid lines are the contour of magnetic flux.

where $\delta\psi = \delta\phi - \frac{T_{i0}}{Z_i n_{i0}}\delta n_i / \left(1 + \frac{e^2}{Z_i^2}\frac{n_{e0}}{n_{i0}}\frac{T_{i0}}{T_{e0}}\right)$, $\rho_s = C_s/\Omega_{ci}$, and $C_s = \sqrt{T_e/m_i}$ is the ion sound speed. By applying the Fourier transform in the toroidal direction to Eq. (31), we have

$$\frac{e^2 n_{i0}}{T_{e0}}\left[-\frac{Z_i^2}{e^2}\rho_s^2\left(1+\frac{e^2}{Z_i^2}\frac{n_{e0}}{n_{i0}}\frac{T_i}{T_e}\right)\nabla_\perp^2(n) + \frac{n_{e0}}{n_{i0}}\right]\delta\psi(n) = Z_i\delta n_i(n)\frac{1}{1+\frac{e^2}{Z_i^2}\frac{n_{e0}}{n_{i0}}\frac{T_{i0}}{T_{e0}}}. \quad (32)$$

For each toroidally spectral component with mode number n, we carry out central finite difference of $\nabla_\perp^2(n)$ as shown by Eqs. (15)–(17) on the (R, Z) plane and construct the tridiagonal matrix on field aligned simulation grids. Then, the sparse discrete matrix equation for Eq. (32) is solved using the Krylov method implemented in PETSc software.

IV. CODE VERIFICATION

A. Slab limit

In this section, we show the benchmark results of GTC-X against the analytical dispersion relation in an approximately uniform magnetic field (ignore the ion diamagnetic and curvature drifts). Applying Fourier transform $\partial_t = -i\omega$, $\boldsymbol{b}_0\cdot\nabla = ik_{||}$, and $\nabla_\perp = i\boldsymbol{k}_\perp$ for Eq. (22) in linear plasmas in a uniform magnetic field, we can derive the linear perturbed distribution of gyrokinetic ion species

$$\delta f_i = \frac{1}{\omega - k_{||}v_{||}}\left\{-\frac{Z_i}{T_i}\omega_i^*\left[1+\left(\frac{m_i v_{||}^2 + 2\mu B_0}{2T_i} - 1.5\right)\eta_i\right] + \frac{Z_i k_{||} v_{||}}{T_i}\right\}\langle\delta\phi\rangle f_{i0}, \quad (33)$$

where $\langle\delta\phi\rangle = \frac{1}{2\pi}\oint\delta\phi(\mathbf{x})d\zeta = \sum_k \delta\phi(\mathbf{k})exp(i\mathbf{k}\cdot\mathbf{R})J_0\left(\frac{k_\perp v_\perp}{\Omega_{ci}}\right)$, $\mathbf{x}$ is the particle position, and $\mathbf{R}$ is the gyrocenter position, $\omega_i^* = \frac{cT_i}{Z_i B_0}\frac{1}{n_{i0}}\frac{\partial n_{i0}}{\partial r}k_\zeta$ is the ion diamagnetic drift frequency (negative value for the normal profile which decreases along the $\hat{R}$ direction), $k_\zeta = n/R$ is the perpendicular wave vector, and $\eta_i = dlnT_i/dlnn_{i0}$. Integrating Eq. (33) to the 0th order, the ion density perturbation becomes

$$\langle\delta n_i\rangle = \left\{-\frac{Z_i n_{i0}}{T_i} - \frac{Z_i n_{i0}}{T_i}\frac{\omega-\omega_i^*}{\omega}\xi_i Z(\xi_i) + \frac{Z_i n_{i0}}{T_i}\eta_i\frac{\omega_i^*}{\omega}\xi_i^2[1+\xi_i Z(\xi_i)] - \frac{3}{2}\frac{Z_i n_{i0}}{T_i}\eta_i\frac{\omega_i^*}{\omega}\xi_i Z(\xi_i)\right\} \times \Gamma_0(k_\perp^2\rho_i^2)\delta\phi + \frac{Z_i n_{i0}}{T_i}\eta_i\frac{\omega_i^*}{\omega}\xi_i Z(\xi_i)\left[(1-k_\perp^2\rho_i^2)\right. \times \left.\Gamma_0(k_\perp^2\rho_i^2) + k_\perp^2\rho_i^2\Gamma_1(k_\perp^2\rho_i^2)\right]\delta\phi, \quad (34)$$

where $\Gamma_0(k_\perp^2\rho_i^2) = I_0(k_\perp^2\rho_i^2)exp(-k_\perp^2\rho_i^2)$, $\Gamma_1(k_\perp^2\rho_i^2) = I_1(k_\perp^2\rho_i^2)exp(-k_\perp^2\rho_i^2)$ and $Z(\xi_i) = \pi^{-1/2}\int_{-\infty}^{+\infty}\frac{dtexp(-t^2)}{t-\xi_i}$ is the plasma function.

Combing Eqs. (34), (25), and (26), we can derive the linear dispersion relation as[15]

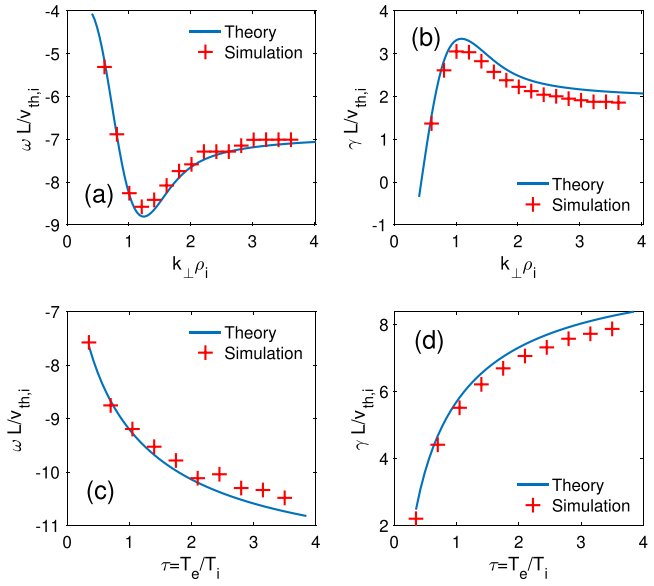

FIG. 5. Frequency and growth rate of the ITG mode dependence on $k_\perp\rho_i$ in panels (a) and (b) and dependence on $\tau = T_e/T_i$ in panels (c) and (d).

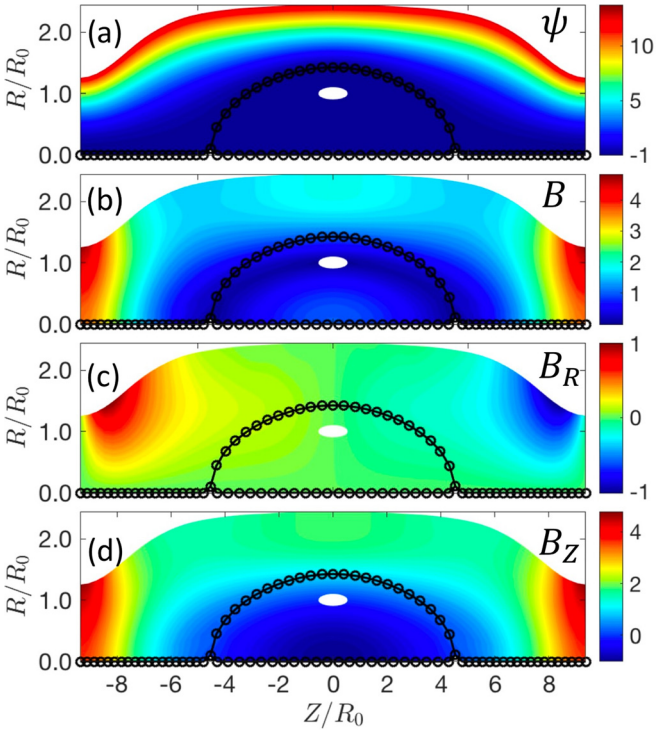

FIG. 6. (a) Magnetic poloidal flux normalized by a separatrix value: $\psi/|\psi_O|$, (b)–(d) are total magnetic field B, radial magnetic field B_R, and axial magnetic field B_Z normalized by $B_0 = 531$ G. The circles represent the separatrix.

$$0 = \left[1 - \Gamma_0\left(k_\perp^2\rho_i^2\right)\right] + \frac{T_i}{T_e}\frac{e^2 n_{e0}}{Z_i^2 n_{i0}} - \eta_i \frac{\omega_i^*}{\omega}\xi_i Z(\xi_i)$$
$$\times \left[\left(1 - k_\perp^2\rho_i^2\right)\Gamma_0\left(k_\perp^2\rho_i^2\right) + k_\perp^2\rho_i^2\Gamma_1\left(k_\perp^2\rho_i^2\right)\right]$$
$$-\left\{-1 - \left(1 - \frac{\omega_i^*}{\omega}\right)\xi_i Z(\xi_i) + \eta_i \frac{\omega_i^*}{\omega}\xi_i^2\left[1 + \xi_i Z(\xi_i)\right]\right.$$
$$\left. -\frac{3}{2}\eta_i \frac{\omega_i^*}{\omega}\xi_i Z(\xi_i)\right\}\Gamma_0\left(k_\perp^2\rho_i^2\right). \quad (35)$$

Next, in order to compare with theory Eq. (35) in the slab limit, we carry out simulations in the domain of Fig. 1: $Z/R_0 \in [-0.2, 0.2]$ and ψ ranges from $\psi(R = 1.702R_0, Z = 0)$ to $\psi(R = 1.705R_0, Z = 0)$, where the magnetic field variation is small and magnetic drift effect can be ignored. In the simulation, $\kappa_{Ti} = \frac{1}{T_i}\frac{\partial T_i}{\partial R}|_{Z=0} = 5.0$, $\kappa_{Te} = \frac{1}{T_e}\frac{\partial T_e}{\partial R}|_{Z=0} = 0.0$, $\kappa_{ni} = \kappa_{ne} = \frac{1}{T_i}\frac{\partial n_i}{\partial R}|_{Z=0} = 2.5$, $\eta_i = \kappa_{Ti}/\kappa_{ni} = 2.0$, and the parallel vector $k_{||}$ is fixed: $k_{||}\rho_i = 1.08 \times 10^{-2}$, and the perpendicular vector is determined by the toroidal component: $k_\perp = k_\zeta$. We first fixed $\tau = T_e/T_i = 0.35$ and scanned $k_\perp\rho_i$ (we use deuterium as ion species in the simulation) by increasing k_ζ; and the simulation results agree well with theory as shown in Figs. 5(a) and 5(b). Then,

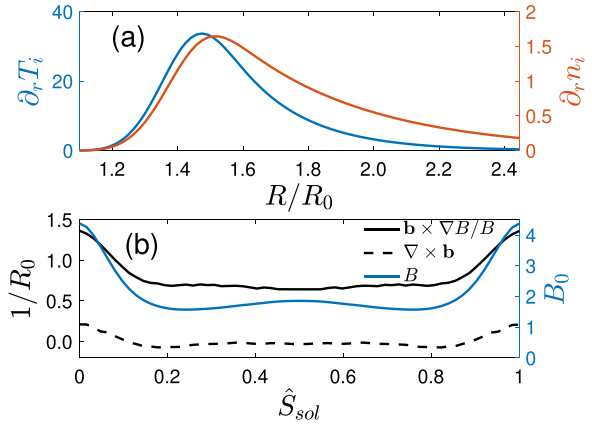

FIG. 7. (a) Ion temperature and density gradients at outer midplane $Z = 0$, where T_i is normalized by electron temperature at the axis $T_{ea} = 80.0$ eV, n_i is normalized by electron density at the axis $n_{ea} = 2.44 \times 10^{13}$ cm^{-3}, and r is normalized by $R_0 = 26.8$ cm. (b) Magnetic field strength B, ∇B, and $\nabla \times \boldsymbol{B}$ scale length along the parallel direction at field line $\psi = \psi(R = 2.02R_0, Z = 0)$.

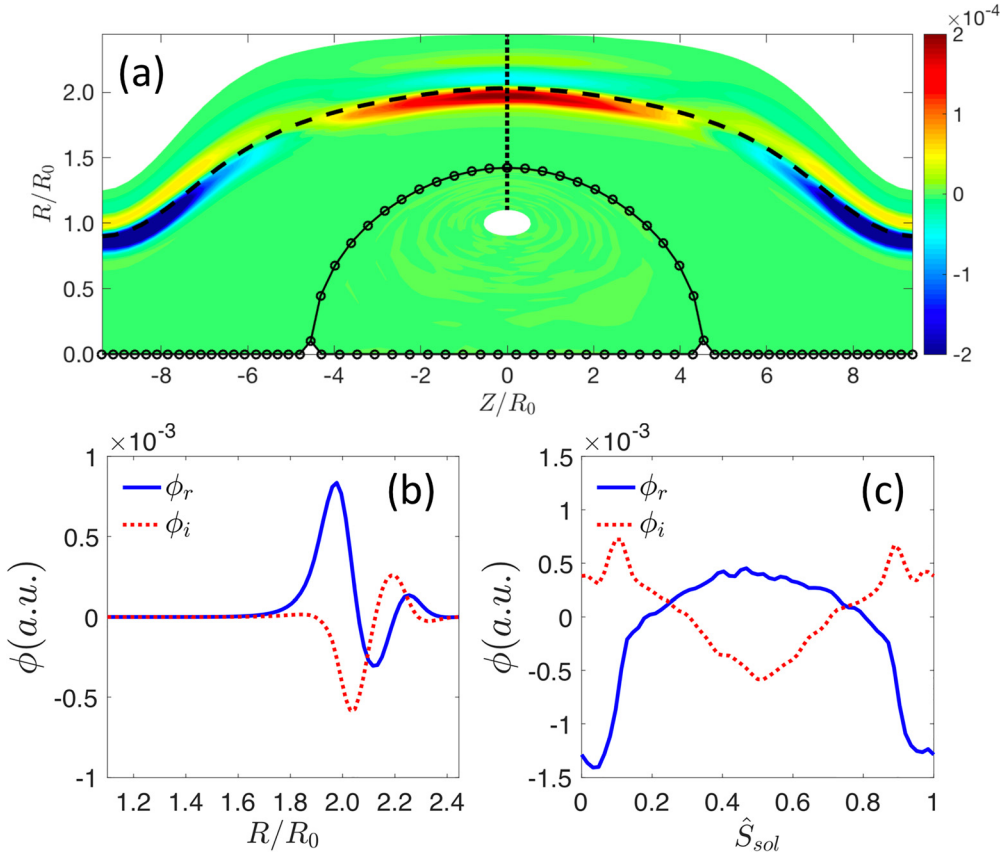

FIG. 8. (a) Electrostatic potential of the ITG mode in FRC. The circles represent the separatrix. The mode structures of real and imaginary parts (b) along the radial direction at the outer midplane ($Z = 0$) as shown by the black dotted line in (a), and the separatrix radial location is $R/R_0 = 1.42$, and (c) along the parallel direction [field line with $\psi(R = 2.02R_0, Z = 0)$ as shown by the black dashed line in (a)].

TABLE I. Parallel domain size effects on the ITG mode.

Domain size	Frequency	Growth rate	Parity of real part	Parity of imaginary part
$Z/R_0 \in [-9.37, 9.37]$	$-0.0108\Omega_{cp}$	$0.0022\Omega_{cp}$	Even	Even
$Z/R_0 \in [-13.6, 13.6]$	$-0.0046\Omega_{cp}$	$0.0046\Omega_{cp}$	Even	Even
$Z/R_0 \in [-16.2, 16.2]$	$-0.0022\Omega_{cp}$	$0.0030\Omega_{cp}$	Even	Even
$Z/R_0 \in [-19.2, 19.2]$	$-0.0052\Omega_{cp}$	$0.0035\Omega_{cp}$	Odd	Odd
$Z/R_0 \in [-21.0, 21.0]$	$-0.0043\Omega_{cp}$	$0.0037\Omega_{cp}$	Odd	Odd

we fixed $k_\perp \rho_i = 2.0$ and scanned τ; and GTC-X simulation results are in good agreement with theory as shown in Figs. 5(c) and 5(d). In Fig. 5, the frequency and growth rate are normalized by $v_{th,i}/L$, where $v_{th,i} = \sqrt{T_i/m_i}$ is the ion thermal speed, and $L = 0.4R_0$ is the parallel length of simulation domain.

B. FRC geometry

Next, we carry out simulation in the middle part of a realistic FRC geometry. The deuterium plasma is simulated in this case which is consistent with experiments.[10] The inner boundary and outer boundary of the simulation domain are $\psi_0 = 0.96\psi_O$ and $\psi_1 = 13.8|\psi_O|$, where ψ_O is the poloidal magnetic flux value at the magnetic axis, $R/R_0 \in [0.0, 2.45]$ in the radial direction at the outer midplane, $Z/R_0 \in [-9.37, 9.37]$ in the axial direction, $R_0 = 26.8$ cm, and the region close to the magnetic axis $\psi \in [0, \psi_0]$ is excluded for the gyrokinetic model validation. Both particle and field boundary conditions at the field line ends ($Z/R_0 = \pm 9.37$) are periodic since the FRC center is far away from the divertor region, where the sheath effect becomes important. In this paper, we do not take into account the presheath and sheath effects on the ITG in the FRC center and formation region. In the radial boundaries, i.e., $\psi = \psi_0$ and $\psi = \psi_1$, we apply the reflected boundary condition for particle and zero boundary condition for fields since the fluctuations of ITG are considered to be zero there. The ψ, B, B_R, and B_Z value are shown in Fig. 6, which are normalized by the magnetic field strength $B_0 = 531$ G at the cross point between the separatrix and the outer midplane: ($R = R_X = 1.42R_0$, $Z = 0$). The ion temperature and density gradients are shown in Fig. 7. We choose to simulate the ITG mode with the toroidal mode number $n = 20$, and the corresponding $k_\zeta \rho_i = 0.36$. The elongated parallel mode structure and finite radial structure of the ITG mode are found in our simulation as shown in Fig. 8, i.e., $k_{||} \ll k_r$ and $k_{||} \ll k_\zeta$, and we can estimate $k_r \rho_i \approx 0.57$. According to the parallel mode structure along the field line $\psi = \psi(R = 2.02R_0, Z = 0)$ as shown in Fig. 8(c), both the real and imaginary parts of electrostatic potential perturbation of $n = 20$ mode are even parity. The frequency and growth rates are $\omega_r = -5.98v_{th,i}/L_S = -0.0108\Omega_{cp}$ and $\gamma = 1.22v_{th,i}/L_S = 0.0022\Omega_{cp}$, where $L_S = 18.8R_0$ is the field line distance between left and right boundaries and $\Omega_{cp} = eB_0/(cm_p)$ is the proton cyclotron frequency. GTC-X simulation of the ITG mode in the local FRC geometry agrees with another gyrokinetic particle code ANC, which gives the result $\omega_{r,ANC} = -5.30v_{th,i}/L_S$ and $\gamma_{ANC} = 1.17v_{th,i}/L_S$.[33,34] The location of the unstable ITG mode is determined by a balance of temperature drive, η_i value, and magnetic drift strength. In FRC, the magnetic gradient drift is opposite to diamagnetic drift, and magnetic curvature drift is the same as the diamagnetic drift in the outer midplane and opposite to diamagnetic drift in mirror throats.

V. GLOBAL GYROKINETIC SIMULATION OF ITG INSTABILITY

In this section, we study the global effects of FRC on the ITG. Using FRC equilibrium as shown in Fig. 1, we choose the parallel domain Z/R_0 as $[-13.6, 13.6]$, $[-16.2, 16.2]$, $[-19.2, 19.2]$, and $[-21.0, 21.0]$, respectively, for simulations of deuterium plasmas. The plasma profile and radial domain are the same with Sec. IV B as shown in Fig. 7(a). We still focus on the $n = 20$ toroidal mode ($k_\zeta \rho_i = 0.36$) and compare the mode structure, frequency, and growth rate among simulations with different parallel domain lengths, which are shown in Table I. The 2D poloidal mode structure and 1D parallel mode

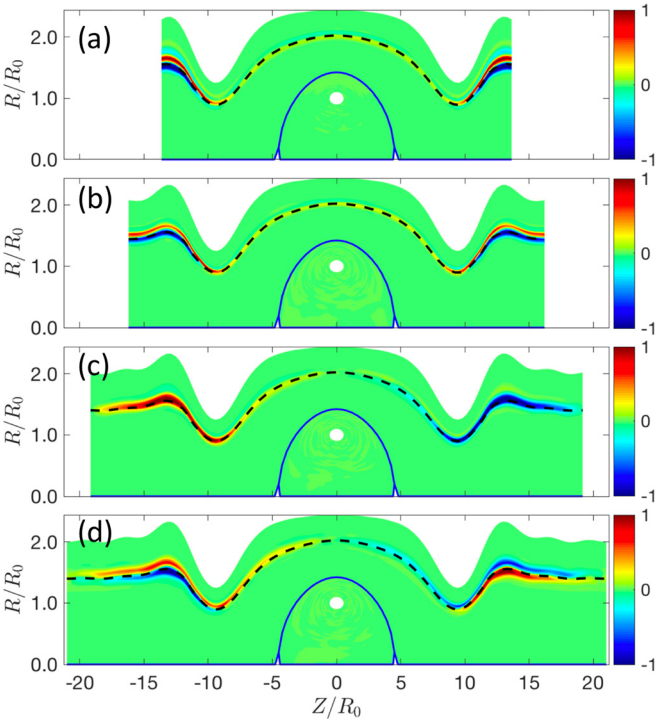

FIG. 9. Comparison of 2D poloidal mode structures of ITG instability between different parallel domain simulations: (a) $Z/R_0 \in [-13.6, 13.6]$, (b) $Z/R_0 \in [-16.2, 16.2]$, (c) $Z/R_0 \in [-19.2, 19.2]$, and (d) $Z/R_0 \in [-21.0, 21.0]$. The dashed lines show the flux surfaces with the maximum mode amplitude. The blue solid line is the separatrix.

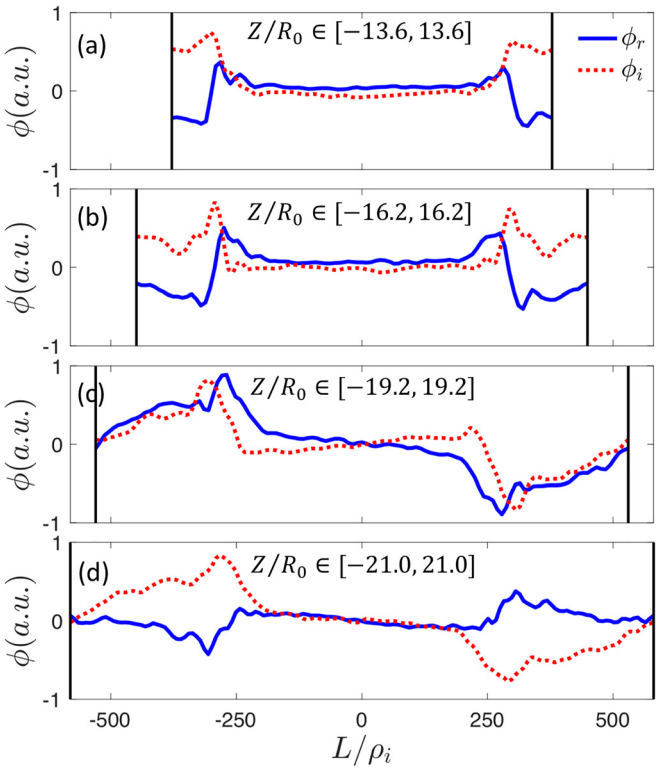

FIG. 10. Comparison of 1D parallel mode structures on the diagnostic flux surfaces between different parallel domain simulations. L/ρ_i is the field line distance normalized by ρ_i at local flux surface. The diagnostic flux surfaces are shown by the dashed lines in Fig. 9.

structure are shown in Figs. 9 and 10, respectively. The global FRC simulation shows that the ITG mode grows along the field line direction with long parallel wavelength mode structure in SOL crossing the regions of the central chamber and formation sections with the transition mirror regions included. The maximum amplitude of this mode is in the formation region with bad curvature. Meanwhile, in central FRC, the amplitude is much lower as shown in Fig. 9. In the core, ITG is stable. This is due to the large electron parallel dynamics, large Larmor radius effect, and large grad-B drift the direction of which is opposite to ion diamagnetic drift.[27] We also find that the ITG parity changes from even to odd by increasing the parallel domain length. For the even parity modes, when increasing the domain size, the frequency shows a down shift, while the growth rate first increases and then decreases, which is caused by the balance between good curvature and bad curvature. The odd parity mode becomes more unstable than the even parity mode by including more formation region ($Z/R_0 \leq -10$ and $Z/R_0 \geq 10$) into the parallel domain, and the frequency and growth rate vary with the domain size. Furthermore, by comparing the mode structures from simulations with different domain sizes, the maximum amplitude location of the modes is in the formation region. From our global gyrokinetic particle simulation, it shows that ITG type drift waves are stable in the core region and unstable in the SOL region in FRC.

VI. CONCLUSIONS

In this paper, we have studied the global dynamics of drift waves in the FRC plasma that consists of various elements such as the closed field FRC central region with its squeezed SOL, strong mirrors, the formation sections, another set of strong mirrors, and divertors. It is important that we can now look at the globally developed drift waves that are extended in the axial direction, while localized only in the SOL region. This study was enabled by developing the global GTC particle model: a new global particle-in-cell code GTC-X. Two sets of coordinates, field line coordinates and cylindrical coordinates, are used in the simulation, which enable the maximum numerical efficiency for cross-separatrix simulation. A field aligned mesh is applied to suppress the unphysical short wave length noise and dramatically decrease the computational cost. GTC-X is well benchmarked with theory and ANC for ITG instability with adiabatic electrons. Global FRC simulations show that the ITG mode is unstable in the SOL distributed along the field line and stable in the core, which is consistent with local simulations and experiments. By extending the simulation domain along the SOL field lines, the parity of the ITG mode changes from even to odd, which shows that the parallel domain size is important for determining the most unstable eigenmode of the drift wave. The nonlinear simulation of ITG transport with kinetic electrons in global FRC geometry will be reported in a future paper.

ACKNOWLEDGMENTS

J.B. and Z.L. would like to acknowledge useful discussions with Dr. L. Shi, Dr. W. L. Zhang, Dr. H. S. Xie, and Dr. Y. Xiao. This work was supported by TAE Grant No. TAE-200441, DOE SciDAC ISEP center, and the Strategic Priority Research Program of Chinese Academy of Sciences under Grant No. XDB16010300. GTC-X simulations used resources on the Oak Ridge Leadership Computing Facility at Oak Ridge National Laboratory (DOE Contract No. DE-AC05-00OR22725) and the National Energy Research Scientific Computing Center (DOE Contract No. DE-AC02-05CH11231).

REFERENCES

[1]M. Tuszewski, "Field reversed configurations," Nucl. Fusion **28**(11), 2033 (1988).
[2]M. W. Binderbauer, H. Y. Guo, M. Tuszewski, S. Putvinski, L. Sevier, D. Barnes, N. Rostoker, M. G. Anderson, R. Andow, L. Bonelli *et al.*, "Dynamic formation of a hot field reversed configuration with improved confinement by supersonic merging of two colliding high-compact toroids," Phys. Rev. Lett. **105**, 045003 (2010).
[3]M. Tuszewski, A. Smirnov, M. C. Thompson, S. Korepanov, and T. Akhmetov, "Field reversed configuration confinement enhancement through edge biasing and neutral beam injection," Phys. Rev. Lett. **108**, 255008 (2012).
[4]M. W. Binderbauer, T. Tajima, L. C. Steinhauer, E. Garate, M. Tuszewski, L. Schmitz, H. Y. Guo, A. Smirnov, H. Gota, D. Barnes *et al.*, "A high performance field-reversed configuration," Phys. Plasmas **22**, 056110 (2015).
[5]H. Y. Guo, M. W. Binderbauer, T. Tajima, R. D. Milroy, L. C. Steinhauer, X. Yang, E. G. Garate, H. Gota, S. Korepanov, A. Necas *et al.*, "Achieving a long-lived high-beta plasma state by energetic beam injection," Nat. Commun. **6**, 6897 (2015).
[6]H. Gota, M. W. Binderbauer, T. Tajima, S. Putvinski, M. Tuszewski, S. Dettrick, E. Garate, S. Korepanov, A. Smirnov, M. C. Thompson *et al.*, "Achievement of field-reversed configuration plasma sustainment via 10 MW neutral-beam injection on the C-2U device," Nucl. Fusion **57**, 116021 (2017).

[7]M. E. Griswold, E. M. Granstedt, M. C. Thompson, K. Knapp, B. Koop, and TAE Team, "Particle and heat flux diagnostics on the C-2W divertor electrodes," Rev. Sci. Instrum. **89**, 10J110 (2018).
[8]D. C. Barnes, J. L. Schwarzmeier, H. Ralph Lewis, and C. E. Seyler, "Kinetic tilting stability of field-reversed configurations," Phys. Fluids **29**, 2616 (1986).
[9]R. Horiuchi and T. Sato, "Full magnetohydrodynamic simulation of the tilting instability in a field-reversed configuration," Phys. Fluids B: Plasma Phys. **1**, 581 (1989).
[10]L. Schmitz, D. P. Fulton, E. Ruskov, C. Lau, B. H. Deng, T. Tajima, M. W. Binderbauer, I. Holod, Z. Lin, H. Gota, M. Tuszewski, S. A. Dettrick, and L. C. Steinhauer, "Suppressed ion-scale turbulence in a hot high-β plasma," Nat. Commun. **7**, 13860 (2016).
[11]S. Gupta, D. C. Barnes, S. A. Dettrick, E. Trask, M. Tuszewski, B. H. Deng, H. Gota, D. Gupta, K. Hubbard, S. Korepanov, M. C. Thompson, K. Zhai, T. Tajima, and TAE Team, "Transport studies in high-performance field reversed configuration plasmas," Phys. Plasmas **23**, 052307 (2016).
[12]M. Onofri, P. Yushmanov, S. Dettrick, D. Barnes, K. Hubbard, and T. Tajima, "Magnetohydrodynamic transport characterization of a field reversed configuration," Phys. Plasmas **24**, 092518 (2017).
[13]L. C. Steinhauer, H. L. Berk, and TAE Team, "Coupled transport in field-reversed configurations," Phys. Plasmas **25**, 022503 (2018).
[14]W. W. Lee, "Gyrokinetic approach in particle simulation," Phys. Fluids **26**, 556 (1983).
[15]W. W. Lee and W. M. Tang, "Gyrokinetic particle simulation of ion temperature gradient drift instabilities," Phys. Fluids **31**(3), 612–624 (1988).
[16]A. M. Dimits and W. W. Lee, "Partially linearized algorithms in gyrokinetic particle simulation," J. Comput. Phys. **107**, 309–323 (1993).
[17]S. E. Parker and W. W. Lee, "A fully nonlinear characteristic method for gyrokinetic simulation," Phys. Fluids B: Plasma Phys. **5**, 77 (1993).
[18]B. I. Cohen, D. C. Barnes, J. M. Dawson, G. W. Hammett, W. W. Lee, G. D. Kerbel, J.-N. Leboeuf, P. C. Liewer, T. Tajima, and R. E. Waltz, "The numerical tokamak project: Simulation of turbulent transport," Comput. Phys. Commun. **87**(1-2), 1–15 (1995).
[19]J. Y. Kim, Y. Kishimoto, M. Wakatani, and T. Tajima, "Poloidal shear flow effect on toroidal ion temperature gradient mode: A theory and simulation," Phys. Plasmas **3**(10), 3689–3695 (1996).
[20]Y. Kishimoto, T. Tajima, W. Horton, M. J. LeBrun, and J. Y. Kim, "Theory of self organized critical transport in tokamak plasmas," Phys. Plasmas **3**(4), 1289–1307 (1996).
[21]Z. Lin, T. S. Hahm, W. W. Lee, W. M. Tang, and R. B. White, "Turbulent transport reduction by zonal flows: Massively parallel simulations," Science **281**, 1835 (1998).
[22]C. S. Chang, S. Ku, P. H. Diamond, Z. Lin, S. Parker, T. S. Hahm, and N. Samatova, "Compressed ion temperature gradient turbulence in diverted tokamak edge," Phys. Plasmas **16**, 056108 (2009).
[23]S. Ethier, C.-S. Chang, S.-H. Ku, W. Lee, W. Wang, Z. Lin, and W. Tang, "NERSCs impact on advances of global gyrokinetic PIC codes for fusion energy research," Comput. Sci. Eng. **17**, 10–21 (2015).
[24]H. S. Xie, Y. Xiao, and Z. Lin, "New paradigm for turbulent transport across a steep gradient in toroidal plasmas," Phys. Rev. Lett. **118**, 095001 (2017).
[25]D. P. Fulton, C. K. Lau, I. Holod, Z. Lin, and S. Dettrick, "Gyrokinetic particle simulation of a field reversed configuration," Phys. Plasmas **23**, 012509 (2016).
[26]D. P. Fulton, C. K. Lau, L. Schmitz, I. Holod, Z. Lin, T. Tajima, M. W. Binderbauer, and TAE Team, "Gyrokinetic simulation of driftwave instability in field-reversed configuration," Phys. Plasmas **23**, 056111 (2016).
[27]C. K. Lau, D. P. Fulton, I. Holod, Z. Lin, M. Binderbauer, T. Tajima, and L. Schmitz, "Drift-wave stability in the field-reversed configuration," Phys. Plasmas **24**, 082512 (2017).
[28]W. Zhang, Z. Lin, and L. Chen, "Transport of energetic particles by microturbulence in magnetized plasmas," Phys. Rev. Lett. **101**, 095001 (2008).
[29]H. S. Zhang, Z. Lin, and I. Holod, "Nonlinear frequency oscillation of Alfven eigenmodes in fusion plasmas," Phys. Rev. Lett. **109**, 025001 (2012).
[30]Z. Wang, Z. Lin, I. Holod, W. W. Heidbrink, B. Tobias, M. Van Zeeland, and M. E. Austin, "Radial localization of toroidicity-induced Alfven eigenmodes," Phys. Rev. Lett. **111**, 145003 (2013).
[31]J. McClenaghan, Z. Lin, I. Holod, W. Deng, and Z. Wang, "Verification of gyrokinetic particle simulation of current-driven instability in fusion plasmas. I. Internal kink mode," Phys. Plasmas **21**, 122519 (2014).
[32]D. Liu, W. Zhang, J. McClenaghan, J. Wang, and Z. Lin, "Verification of gyrokinetic particle simulation of current-driven instability in fusion plasmas. II. Resistive tearing mode," Phys. Plasmas **21**, 122520 (2014).
[33]C. K. Lau, "Electrostatic turbulence and transport in the field-reversed configuration," Ph.D. dissertation (University of California, Irvine, 2017).
[34]C. K. Lau, D. P. Fulton, J. Bao, Z. Lin, T. Tajima, L. Schmitz, and TAE Team, "First simulations of turbulent transport in the field-reversed configuration," in *Proceedings of the 26th International Conference on Plasma Physics and Controlled Nuclear Fusion Research*, Ahmedabad (International Atomic Energy Agency, Vienna, Austria, 2018), Paper No. IAEA-CN-258/TH/p6-37.
[35]S. Ethier, W. Tang, and Z. Lin, "Gyrokinetic particle-in-cell simulations of plasma microturbulence on advanced computing platforms," J. Phys.: Conf. Ser. **16**, 1–15 (2005).
[36]Y. Nishimura and Z. Lin, "A finite element mesh in a tokamak edge geometry," Plasma Phys. **46**(7–9), 551–556 (2006).
[37]L. Galeotti, D. C. Barnes, F. Ceccherini, and F. Pegoraro, "Plasma equilibria with multiple ion species: Equations and algorithm," Phys. Plasmas **18**, 082509 (2011).
[38]Y. Xiao, I. Holod, Z. Wang, Z. Lin, and T. Zhang, "Gyrokinetic particle simulation of microturbulence for general magnetic geometry and experimental profiles," Phys. Plasmas **22**, 022516 (2015).
[39]R. B. White and M. S. Chance, "Hamiltonian guiding center drift orbit calculation for plasmas of arbitrary cross section," Phys. Fluids **27**, 2455 (1984).
[40]A. J. Brizard, "On the validity of the guiding-center approximation in the presence of strong magnetic gradients," Phys. Plasmas **24**, 042115 (2017).
[41]Y. Hayakawa, T. Takahashi, and Y. Kondoh, "Classification of particle orbits and related stochasticity of plasma ion motion in a field-reversed configuration with D3 He advanced fuel," Nucl. Fusion **42**, 1075–1084 (2002).